AIAA JOURNAL
Vol. 38, No. 12, December 2000

Divergence-Free Bases and Multiresolution Methods for Reduced-Order Flow Modeling

Jeonghwan Ko*
Texas A&M University, College Station, Texas 77843-3141
Andrew J. Kurdila†
University of Florida, Gainesville, Florida 32611-6250
and
Othon K. Rediniotis‡
Texas A&M University, College Station, Texas 77843-3141

Although reduced-order modeling methods have flourished in the study of structural system dynamics, similar methodologies for the representation of flow are few in comparison. A novel methodology based on biorthogonal wavelet constructions and multiresolution analysis for order reduction of velocity fields obtained via digital particle image velocimetry or computational fluid dynamics is presented. The derivation, algorithmic implementation, and experimental verification of fast projective filtering methods based on divergence-free wavelets are discussed. Experimental evidence presented demonstrates the feasibility of achieving several hundredfold compression for typical velocity fields obtained via experiments using particle image velocimetry. The results also suggest the feasibility and amenability of wavelet methods for diverse problems of interest to the aerospace community including 1) experimental data denoising, 2) local cross-correlation calculations, and 3) feature extraction.

Introduction

SINCE the introduction of families of compactly supported, orthogonal wavelets by Daubechies,[1] there has been increasing interest in applying wavelet analysis and corresponding time-frequency analysis to engineering problems. A large body of literature has been generated over the recent years on wavelet and multiresolution analysis, with emphasis on signal processing applications. For representative overviews the reader is referred to Refs. 2 and 3. Simply put, wavelet functions have unique properties that enable fast, efficient representation of a large class of functions. One of the most important characteristics of wavelet functions is their simultaneous time-frequency localization. That is, the functions are concentrated not only in the time (or space) domain, but also in the frequency domain. In comparison, it is well known that the conventional Fourier basis functions are locally supported in frequency, but are distributed over the entire real line. Not surprisingly, these localization characteristics have made wavelet-based methods draw immediate attention in signal and image processing areas for better localized filtering and compression. It is now widely accepted that wavelet-based methods provide excellent, high-accuracy compression of scalar functions. In fact, it is possible to characterize metrics by which wavelets define optimal compression methods for signals and images[4] while retaining important features of the original data. There already exist commercially available pieces of software and hardware utilizing wavelet analyses, most notably for scalar-valued functions (signals and images).

Stimulated by the successful applications in these areas, there have been many attempts to utilize wavelet theory in problems of mechanics. The most notable application in computational mechanics has been the use of wavelet functions for approximation of solutions of partial differential equations. The time-frequency localization characteristic provides an asymptotically optimal preconditioning method for obtaining solutions of the associated discretized equations.[5] The localization property also enables effective detection and analysis of singularities in problems governed by partial differential equations.[5] Even more recently, the wavelet method has been applied to particle image velocimetry (PIV) in Ref. 6. The particle images are first wavelet filtered, then velocity distributions are calculated via a wavelet-based windowed cross-correlation algorithm. Compared to an existing Fourier-based PIV method, the wavelet method was shown to provide an efficient and more accurate way to compute velocity fields from PIV. Another successful application of wavelet analysis is the modeling of fluid turbulence in Ref. 7. The coherent structures of turbulence are extracted, and low-dimensional models for the description of turbulence are obtained utilizing wavelet thresholding. With these successes in hand, we present a novel application of the wavelet analysis to the problem of determining reduced-order flow models.

A typical fluid model comprises nonlinear partial differential equations, and significant computational resources are required for their accurate simulation. Although there have been significant advances in computational fluid dynamics (CFD) for faster and more accurate solutions, obtaining the solutions of general, time-dependent flowfields is not an easy task. Moreover, it is clear that the derivation and validation of a flow control methodology will require a considerable amount of computational effort beyond forward integration of the Navier–Stokes equations. The reader is referred to Ref. 8, or the references therein, for a detailed discussion of the computationally expensive costate formulations or iterative optimization methods typically encountered in the control of flow. From a practical standpoint, a controller developed for a specific flow control task will often have to be implemented in real time. Transition[9,10] and turbulence[11] control problems are typical such cases. The order of the controller determines the number of ordinary differential equations that have to be integrated in real time to solve for the state-space variables. For example, in a typical technique for linear transition control of plane Poiseuille flow, considering N wavenumbers and M Chebyshev modes results in $2N(M+1)$ states. To achieve an accurate representation of the flow dynamics, N and M cannot be small. Even for the modest case of $N = M = 10$, we have a system of order 220. In Ref. 10, N and M were chosen to be 32 and 124, respectively, to achieve an adequate approximation and resulted in a system with over 8000 states. Such a large-order system is unrealistic for real-time control applications due to computer hardware and software limitations. In Ref. 10, order reduction was achieved by transforming the system into Jordan canonical

Received 21 October 1998; revision received 1 July 1999; accepted for publication 2 May 2000.

*Postdoctoral Research Associate, Department of Aerospace Engineering; ko@aero.tamu.edu. Member AIAA.
†Associate Professor, Department of Aerospace Engineering, Mechanics and Engineering Science; ajk@aero.ufl.edu. Member AIAA.
‡Assistant Professor, Department of Aerospace Engineering; rediniotis@tamu.edu. Member AIAA.

form and retaining only the states that are equally well controllable and observable, resulting in a reduced-order system with about 600 states. Therefore, about an order of magnitude of order reduction was achieved. The preceding is intended to exemplify the need for reliable order-reduction methodologies that render real-time control technologically feasible, while still reliably retaining the underlying dynamics of the flow to be controlled.

To alleviate such difficulties in computation, several novel order-reduction methods have been introduced so far. One of the most notable methodologies is the proper orthogonal decomposition (POD). The method was originally suggested independently by different scientists, amongst which Loeve[12] and Karhunen[13] are the most recognized. This technique has been applied in fluid mechanics in 1970, when Lumley[14] suggested that POD is amenable for the representation of coherent structures in turbulence. Since then, it has found applications in reduced-order flow modeling and control.[15–20] Briefly, in POD, snapshots of a flowfield at different time and/or at different parameter values are utilized for the generation of basis functions, specific to the flowfield of interest. Out of this initially large basis, typically only a small number of basis elements carry most of the information in the particular flowfield and can thus be used for its reconstruction. This is briefly the principle on which order reduction via POD is based.[15–20] The reduced-order model can then be used as a system model in deriving subsequent control strategies. Typical order reductions achieved via POD in control applications and reported in the relevant literature vary around one order of magnitude (for example, 20 to 1 in Ref. 16, 25 to 1 in Ref. 15).

Herein, we propose a different approach to order reduction: a wavelet-based flowfield compression technique, with the ultimate objective of utilizing the resultant reduced-order modeling for incompressible flow control. Recently derived divergence-free wavelet functions are used to represent the velocity vector fields, and the flowfield is compressed via wavelet decomposition while retaining the physically salient features of the flow. As shown in preliminary results, the compression ratios obtainable from wavelet-based methods can be quite large, more than two orders of magnitude. We seek to achieve significant reduction in required computational resources when this method is used in active flow control.

We emphasize that this paper presents a novel method for the analysis of flowfields obtained from either particle image velocimetry or CFD. Although the techniques presented in this paper could be used for a host of other end uses including denoising and coherent feature extraction, we plan to utilize the reduced-order vector fields for control simulation and design. Because of length limitations, the flow control simulation and design problem is treated in a forthcoming paper. Still, it is important to realize that this target problem imposes special constraints on our PIV compression algorithm: We seek reduced-order divergence-free vector fields.

Problem Framework

To better understand the implications of seeking to generate reduced-order models from PIV for flow simulation, we consider viscous, incompressible flows governed by the Navier–Stokes equations

$$\begin{aligned} \frac{\partial \boldsymbol{u}}{\partial t} - \nu\Delta\boldsymbol{u} + \boldsymbol{u}\cdot\nabla\boldsymbol{u} + \nabla p = \boldsymbol{f} \qquad &\text{in} \qquad \Omega\times(0,T] \\ \nabla\cdot\boldsymbol{u} = 0 \qquad &\text{in} \qquad \Omega\times(0,T] \\ \boldsymbol{u} = \boldsymbol{g} \qquad &\text{on} \qquad \Gamma\times[0,T] \\ \boldsymbol{u}(0,\boldsymbol{x}) = \boldsymbol{u}_0(\boldsymbol{x}) \qquad &\text{in} \qquad \Omega \end{aligned} \tag{1}$$

In these equations $\boldsymbol{u}$ is the velocity field in the domain Ω, Γ is the boundary of the domain, p is the pressure, and ν is the kinematic viscosity. For flow control simulation, it is often convenient to consider the weak form of these equations in which we seek a velocity field $\boldsymbol{u}$ and pressure field p such that

$$\left[\frac{\partial \boldsymbol{u}}{\partial t}(t), \boldsymbol{v}\right] + a[\boldsymbol{u}(t),\boldsymbol{v}] + b[\boldsymbol{u}(t),\boldsymbol{u}(t),\boldsymbol{v}] - c[\boldsymbol{v}, p(t)] = [\boldsymbol{f}(t),\boldsymbol{v}]$$

$$c[\boldsymbol{u}(t), q] = 0 \tag{2}$$

holds for all suitably chosen test functions $\boldsymbol{v}$ and q (see Gunzburger[21] for the complete functional analytic framework and for the definition of $a[\cdot,\cdot]$, $b[\cdot,\cdot,\cdot]$, $c[\cdot,\cdot]$). Typical finite element discretizations of these equations might generate solutions that are expressed in millions of unknowns. For control purposes, it is impractical to consider optimization over such large number of unknowns, and reduced-order models are sought. A common technique[21–24] defines a library of representative basis velocity fields

$$\boldsymbol{U}_{N_R} = \text{span}\left\{\boldsymbol{u}_1, \boldsymbol{u}_2, K, \boldsymbol{u}_{N_R}\right\} \tag{3}$$

where N_R is the number of reduced states. By definition, N_R is much smaller than the number of degrees of freedom for a full model. It is not difficult to show that, provided the library $\boldsymbol{U}_{N_R}$ comprises divergence-free functions, the weak formulation for a reduced-order model can be stated as follows. Find $\boldsymbol{u}_R \in \boldsymbol{U}_{N_R}$ such that

$$\left[\frac{\partial \boldsymbol{u}_R}{\partial t}(t), \boldsymbol{v}\right] + a[\boldsymbol{u}_R(t),\boldsymbol{v}] + b[\boldsymbol{u}_R(t),\boldsymbol{u}_R(t),\boldsymbol{v}] = [\boldsymbol{f}(t),\boldsymbol{v}] \tag{4}$$

for all $\boldsymbol{v}$ in $\boldsymbol{U}_{N_R}$, subject to suitable boundary conditions. The treatment of boundary conditions is an interesting problem in its own right; the readers may see Ref. 21 for details. The resulting low-order system of ordinary differential equations is particularly well suited for control optimization because the pressure term does not appear.

It is emphasized that although the basic theory of reduced-order modeling is exploited via CFD, the method is generic such that it can equally be applied to experimentally obtained data. Specifically, the critical step of constructing a reduced-order model is to generate the reduced-order basis library $\boldsymbol{U}_{N_R}$ in Eq. (3), and, in most cases, the library is obtained by postprocessing either CFD solutions or experimentally obtained PIV flowfields. In this paper, we seek to generate the library $\boldsymbol{U}_{N_R}$ from experimental methods and forego CFD altogether. From an experimental standpoint, this is highly desirable because full field velocity measurements are obtainable at least in principle. Full field pressure measurements are much more difficult, if not impossible, to obtain. The purpose of this paper, then, is the definition of a methodology for generating the reduced-order representations in $\boldsymbol{U}_{N_R}$.

Multiresolution Analyses and Biorthogonal Wavelets

Even for simple applications in which we seek to employ divergence-free wavelets in two dimensions, as is required in the treatment of the PIV data in the final section of this paper, the theory of multiresolution analysis can be intimidating. In this section, we quickly review only those facets of multiresolution analysis that are needed to construct divergence-free bases and perform order reduction in the context of PIV. The interested reader is referred to the numerous monographs on the foundations of this topic (see, for example, Cohen et al.[25]). In its simplest form, a multiresolution analysis is a sequence of nested spaces

$$\cdots V_{-2} \subset V_{-1} \subset V_0 \subset V_1 \subset V_2 \subset \cdots \subseteq L^2(\boldsymbol{R}) \tag{5}$$

that is generated from a single scalar-valued function $\phi(x)$. The function $\phi(x)$ is known as the scaling function, or generator, of the multiresolution analysis. As usual, $L^2(\boldsymbol{R})$ denotes those functions that are square integrable over the real line. Let $\boldsymbol{Z}$ denote the (signed) integers. Each space V_j is defined in terms of the scaling function as

$$V_j = \underset{k\in Z}{\text{span}}\{\phi(2^j x - k)\} \tag{6}$$

Note that the frequency of the generating functions 2^j is fixed in each space V_j. The space V_j is obtained by taking all translations of the generating functions. If we picture the generator $\phi(x)$ as a bump function (see Figs. 1a, 1b, and 1e) supported on a mesh size 2^{-j}, we can view the sequence of spaces V_j as being able to represent functions on grids that are successively refined by a factor of one-half. A pair of multiresolution analyses $\{V_j\}_{j\in Z}$ and $\{\tilde{V}_j\}_{j\in Z}$

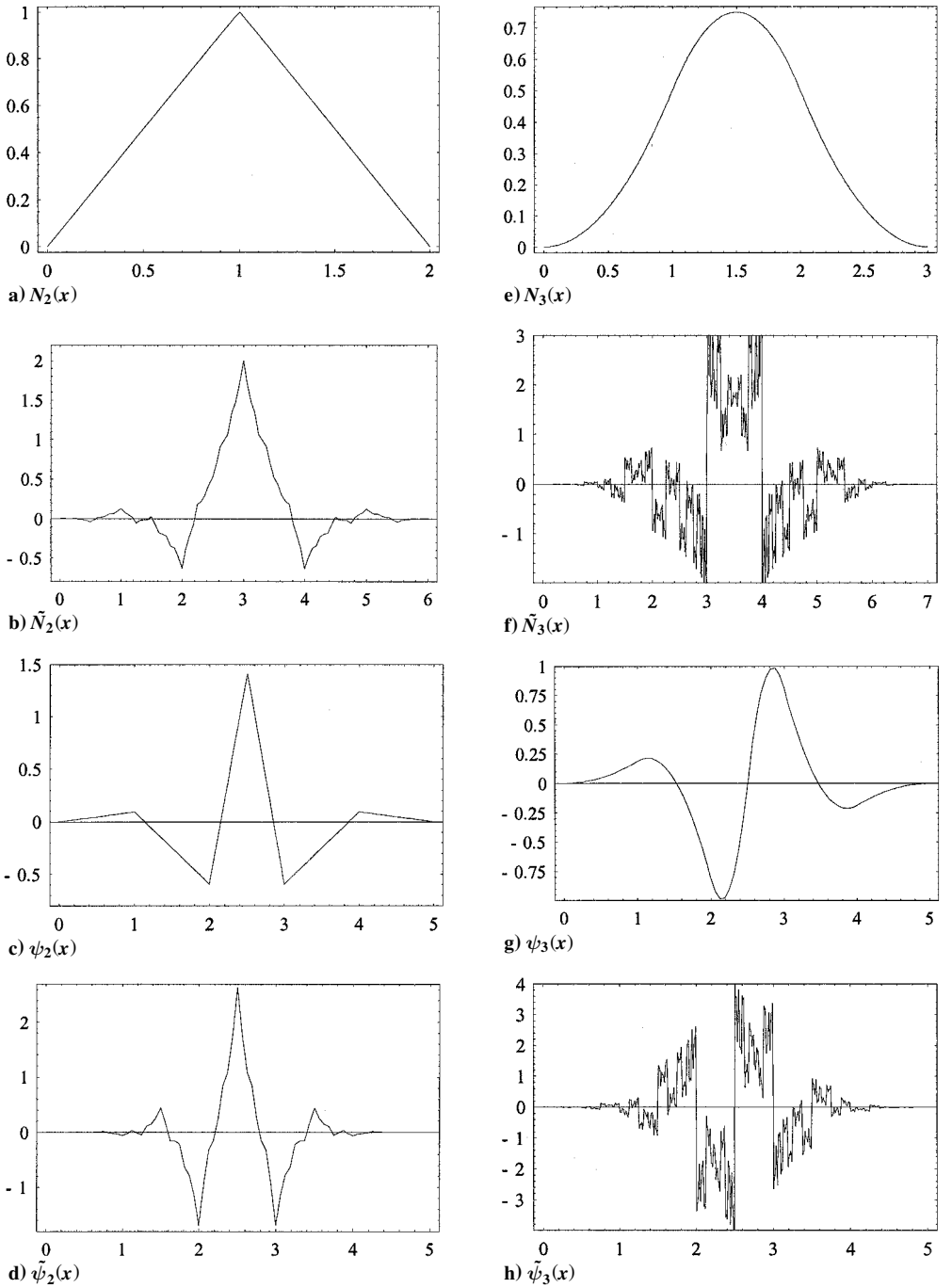

Fig. 1 Families of biorthogonal B-spline functions.

is said to be biorthogonal if their associated scaling functions ϕ and $\tilde{\phi}$ are biorthogonal in the sense that

$$\langle \phi, \tilde{\phi}(\cdot - k) \rangle = \int_R \phi(x)\tilde{\phi}(x-k)\,\mathrm{d}x = \delta_{0,k} \tag{7}$$

Given a biorthogonal pair of multiresolution analyses $\{V_j\}_{j \in Z}$ and $\{\tilde{V}_j\}_{j \in Z}$, we define the (oblique) projectors

$$P_j : L^2(\boldsymbol{R}) \rightarrow V_j, \qquad P_j f = \sum_k \langle f, \phi^{\%}_{j,k} \rangle \phi_{j,k}(x) \tag{8}$$

where

$$\phi_{j,k}(x) = 2^{j/2}\phi(2^j x - k), \qquad \tilde{\phi}_{j,k}(x) = 2^{j/2}\tilde{\phi}(2^j x - k) \tag{9}$$

Thus, by convention, j denotes the dilation (or scaling) of a basis function, and k denotes the translation of a function. The normalization by $2^{j/2}$ simply enforces orthonormality on all levels:

$$\langle \phi_{j,k}, \tilde{\phi}_{j,m} \rangle = \int_R \phi_{j,k}(x)\tilde{\phi}_{j,m}(x)\,\mathrm{d}x = \delta_{k,m} \tag{10}$$

By the definition of P_j and the biorthogonality property, it is true that

$$\langle P_j f, g \rangle = 0, \qquad \forall g \in \tilde{V}_j \tag{11}$$

We say that P_j is the (oblique) projector from $L^2(\boldsymbol{R})$ onto V_j in the direction perpendicular to $\tilde{V}_j$. In the derivation of divergence-free wavelets, we will likewise have occasion to use the oblique projectors onto the complement spaces W_j, which are defined to be

$$Q_j = P_{j+1} - P_j : L^2(\boldsymbol{R}) \rightarrow W_j \tag{12}$$

where

$$W_j = V_{j+1} \cap (\tilde{V}_j)^{\perp} \tag{13}$$

It can be shown that

$$Q_j f = \sum_k \langle f, \tilde{\psi}_{j,k} \rangle \psi_{j,k}(x) \tag{14}$$

where $\psi_{j,k}(x) = 2^{j/2}\psi(2^j x - k)$, $\tilde{\psi}_{j,k}(x) = 2^{j/2}\tilde{\psi}(2^j x - k)$, and ψ and ψ are the biorthogonal wavelets associated with ϕ and $\tilde{\phi}$, respectively. In this paper, the multiresolution analyses will be defined in terms of the specific two scale relations

$$\phi(x) = \sum_k a_k \phi(2x - k), \qquad \tilde{\phi}(x) = \sum_k \tilde{a}_k \tilde{\phi}(2x - k) \tag{15}$$

satisfied by the generators ϕ and $\tilde{\phi}$. Throughout this paper we will assume that the generators are compactly supported (i.e., they are nonzero only on a closed and bounded set and zero otherwise) and, consequently, that the summation in these equations is necessarily finite. It will frequently be convenient to consider the Fourier transform, or Z transform, of the two-scale equations, in which case we obtain

$$a(\xi) = \sum_{k \in Z} a_k e^{-ik\xi}, \qquad a(z) = \sum_{k \in Z} a_k z^k \tag{16}$$

All of the fast projective (filtering) operations discussed in this paper can be carried out in terms of the coefficient sequences $\{a_k\}$ and $\{\tilde{a}_k\}$. The reader is referred to Daubechies[26] for a detailed discussion.

Divergence-Free Wavelets

The original derivation of divergence-free wavelets is due to Lemarie-Rieusset[27–29] and employs tensor product constructions of biorthogonal wavelets. Urban[30,31] generalizes this methodology to create constructions of divergence-free wavelets that are not restricted to tensor products. Because we will deal exclusively with two-dimensional frames of data generated from particle image velocimetry, the framework of Lemarie-Rieusset[27–29] will be sufficient in this paper, that is, there is no compelling reason to utilize divergence-free wavelets that are not tensor products. The purpose of this section is to provide a brief technical background, define the specific dual bases we employ in our PIV applications, and to give precise algorithmic details required for implementation.

We emphasize that this section has been carefully written to provide a concise self-contained, accessible explanation of the methodology presented in Refs. 27–29 to construct divergence-free wavelets. The details of this section will be required by those researchers who seek to implement the PIV postprocessing and filtering algorithms introduced in the next two sections. A casual reader, who only seeks to evaluate the performance of the algorithms on experimental PIV data, may skip to Eq. (49), which summarizes the form of the projection appropriate for multiresolution analysis via divergence-free wavelets. Comments following Eq. (49) describe how all of the constituents of the projector can be expressed in terms of finite impulse response filters.

The essential ingredient in the construction of divergence-free wavelets is the following result due to Lemarie-Rieusset.[27–29]

Proposition: Suppose that $\{V_j\}$ and $\{\tilde{V}_j\}$ are biorthogonal multiresolution analyses with associated generators ϕ and $\tilde{\phi}$ and wavelets ψ and $\tilde{\psi}$. Then there are dual scaling functions ϕ_+ and ϕ_- that define biorthogonal multiresolution analyses $\{V_{-,j}\}$ and $\{V_{+,j}\}$ that are related by integration and differentiation in the sense that

$$\frac{d\phi}{dx}(x) = \phi_-(x) - \phi_-(x-1) \tag{17}$$

$$\int_x^{x+1} \tilde{\phi}(s)\, ds = \phi_+(x) \tag{18}$$

Moreover, if the Laurent series symbol for ϕ and $\tilde{\phi}$ are $a(z)$ and $\tilde{a}(z)$, respectively, then the symbols for ϕ_+ and ϕ_- are given by

$$a_-(z) = [2/(1+z)]a(z) \tag{19}$$

$$a_+(z) = [(1+\bar{z})/2]a(z) \tag{20}$$

If ψ and $\tilde{\psi}$ and ψ_+ and ψ_- denote the biorthogonal wavelets corresponding to ϕ and $\tilde{\phi}$ and ϕ_+ and ϕ_-, respectively, we have

$$\psi_-(x) = \frac{1}{4}\frac{d\psi}{dx}(x) \tag{21}$$

$$\frac{d}{dx}[\psi_+(x)] = -4\tilde{\psi}(x) \tag{22}$$

The choice of subscripts + and − on the dual scaling functions ϕ_+ and ϕ_- arise from Eqs. (17) and (18); the function ϕ_- is defined in terms of the derivative of ϕ, whereas ϕ_+ is defined in terms of the integral of $\tilde{\phi}$. Clearly, Eqs. (17) and (18) can be replaced by the alternative equations

$$\frac{d\phi}{dx}(x) = \phi_-(x) - \phi_-(x-1) \tag{23}$$

$$\frac{d}{dx}[\phi_+(x)] = \tilde{\phi}(x+1) - \tilde{\phi}(x) \tag{24}$$

which illustrate that there is a certain symmetry in the roles of the scaling functions ϕ_+ and ϕ_-. We will use this form of the equations frequently in the derivations that follow.

The construction of divergence-free wavelets is carried out by defining the vector space of tensor products

$$\boldsymbol{V}_j = \begin{Bmatrix} V_j \otimes V_{-,j} \\ V_{-,j} \otimes V_j \end{Bmatrix} \tag{25}$$

Because by definition we have

$$V_{-,j} = \text{span}\{\phi_{-,j,k}\}, \qquad V_j = \text{span}\{\phi_{j,k}\} \tag{26}$$

it is clear that the vector space of tensor products is just a span of one-dimensional subspaces given as

$$\boldsymbol{V}_j = \begin{Bmatrix} V_j \otimes V_{-,j} \\ V_{-,j} \otimes V_j \end{Bmatrix} = \operatorname*{span}_{k,l} \begin{Bmatrix} \phi_{j,k}(x)\phi_{-,j,l}(y) \\ 0 \end{Bmatrix} \oplus \operatorname*{span}_{k,l} \begin{Bmatrix} 0 \\ \phi_{-,j,k}(x)\phi_{j,l}(y) \end{Bmatrix} \tag{27}$$

We emphasize that the symbol $\oplus$ denotes the direct sum, and not an orthogonal sum, throughout this paper. Our primary goal is to find a multilevel decomposition for the vector space $\boldsymbol{V}_j$. This decomposition can be achieved by noting that

$$V_{-,j} = V_{-,j-1} \oplus W_{-,j-1}, \qquad V_j = V_{j-1} \oplus W_{j-1} \tag{28}$$

An explicit, multilevel decomposition of all vectors in $\boldsymbol{V}_j$ can be readily obtained

$$\begin{aligned} \boldsymbol{V}_j = \operatorname*{span}_{k,l} \Bigg\{ & \begin{Bmatrix} \phi_{j-1,k}(x)\phi_{-,j-1,l}(y) \\ 0 \end{Bmatrix}, \begin{Bmatrix} \phi_{j-1,k}(x)\psi_{-,j-1,l}(y) \\ 0 \end{Bmatrix}, \\ & \begin{Bmatrix} \psi_{j-1,k}(x)\phi_{-,j-1,l}(y) \\ 0 \end{Bmatrix}, \begin{Bmatrix} \psi_{j-1,k}(x)\psi_{-,j-1,l}(y) \\ 0 \end{Bmatrix} \\ & + \begin{Bmatrix} 0 \\ \phi_{-,j-1,k}(x)\phi_{j-1,l}(y) \end{Bmatrix}, \begin{Bmatrix} 0 \\ \phi_{-,j-1,k}(x)\psi_{j-1,l}(y) \end{Bmatrix}, \\ & \begin{Bmatrix} 0 \\ \psi_{-,j-1,k}(x)\phi_{j-1,l}(y) \end{Bmatrix}, \begin{Bmatrix} 0 \\ \psi_{-,j-1,k}(x)\psi_{j-1,l}(y) \end{Bmatrix} \Bigg\} \end{aligned} \tag{29}$$

In particular, the complement spaces of vector-valued wavelets is most important. We will use these spaces to decompose the PIV data

vectors for order-reduction, denoising, or cross-correlation calculations:

$$\boldsymbol{W}_{j-1} \equiv \boldsymbol{V}_j \boldsymbol{e} \boldsymbol{V}_{j-1} = \operatorname*{span}_{k,l} \left\{ \begin{Bmatrix} \phi_{j-1,k}(x)\psi_{-,j-1,l}(y) \\ 0 \end{Bmatrix}, \begin{Bmatrix} \psi_{j-1,k}(x)\phi_{-,j-1,l}(y) \\ 0 \end{Bmatrix}, \begin{Bmatrix} \psi_{j-1,k}(x)\psi_{-,j-1,l}(y) \\ 0 \end{Bmatrix} + \begin{Bmatrix} 0 \\ \phi_{-,j-1,k}(x)\psi_{j-1,l}(y) \end{Bmatrix}, \begin{Bmatrix} 0 \\ \psi_{-,j-1,k}(x)\phi_{j-1,l}(y) \end{Bmatrix}, \begin{Bmatrix} 0 \\ \psi_{-,j-1,k}(x)\psi_{j-1,l}(y) \end{Bmatrix} \right\} \tag{30}$$

Hence, our task is then to find a basis for those vectors in the complement spaces that are divergence free. It is convenient to employ the following notation to simplify the representation of divergence-free vectors that live in the space $\boldsymbol{V}_j$:

$$E = \{(e_1, e_2) : e_i \in \{0, 1\}\}, \qquad E^* = E \sim (0, 0) \tag{31}$$

where the symbol $\sim$ implies except. With these sets, we can enumerate a basis for tensor product wavelets as

$$\psi_e = \begin{cases} \psi(x)\phi(y), & e = (1, 0) \\ \phi(x)\psi(y), & e = (0, 1) \\ \psi(x)\psi(y), & e = (1, 1) \end{cases} \tag{32}$$

$$i_e = \min\{i : e_i \neq 0, e_i \in e\} \tag{33}$$

We see that the entries of the vectors in Eq. (30) can almost be expressed in terms of ψ_e. What remains is to select between the multiresolution analyses

$$\{V_j\}_{j \in z}, \qquad \{\tilde{V}_j\}_{j \in z}$$

with generators ϕ and $\tilde{\phi}$ and

$$\{V_{-,j}\}_{j \in z}, \qquad \{V_{+,j}\}_{j \in z}$$

with generators ϕ_- and ϕ_+ in each component of the basis vectors. A superscript is used to denote a coordinate direction in which generators (or wavelets) associated with $\{V_{-,j}\}$ are substituted in the bases ψ_e. In other words, whereas we have

$$\psi_{(1,0)} = \psi(x)\phi(y), \qquad \psi_{(0,1)} = \phi(x)\psi(y), \qquad \ldots \tag{34}$$

for the usual bases, we write

$$\psi^{(1)}_{(1,0)} = \psi_-(x)\phi(y), \qquad \psi^{(2)}_{(1,0)} = \psi(x)\phi_-(y), \qquad \ldots \tag{35}$$

for bases that have been modified in a particular coordinate direction by substituting a basis function from $\{V_{-,j}\}$. This construction can be repeated. If we modify two coordinate directions, we denote $\psi^{(1,2)}_{(1,0)} = \psi_-(x)\phi_-(y)$, as an example. This notation gives a succinct method for representing various projections, decompositions, and reconstructions in the vector bases. For example, the projection onto the tensor product space of scalar-valued functions in $V_j \otimes V_{-,j}$ is just

$$f \mapsto \sum_{k,l} \left[\int_{R^2} \tilde{\phi}_{j,k}(x)\phi_{+,j,l}(y) f(x, y)\, dx\, dy \right] \phi_{j,k}(x)\phi_{-,j,l}(y)$$

$$= \sum_{k,l} \langle f, \tilde{\phi}_{j,k} \otimes \phi_{+,j,l} \rangle \phi_{j,k}(x)\phi_{-,j,l}(y) \tag{36}$$

We define the scalar projection

$$f \mapsto Q^{(2)}_j f = \sum_{k,l} \langle f, \tilde{\phi}_{j,k} \otimes \phi_{+,j,l} \rangle \phi_{j,k}(x)\phi_{-,j,l}(y) \tag{37}$$

The definition of projections of vector-valued functions onto vector-valued tensor product spaces is defined using the scalar-valued projections:

$$\begin{Bmatrix} f_1 \\ f_2 \end{Bmatrix} \mapsto \begin{Bmatrix} Q^{(2)}_j f_1 \\ Q^{(1)}_j f_2 \end{Bmatrix} = \begin{Bmatrix} \sum_{k,l} \langle f_1, \tilde{\phi}_{j,k} \otimes \phi_{+,j,l} \rangle \phi_{j,k}(x)\phi_{-,j,l}(y) \\ \sum_{k,l} \langle f_2, \tilde{\phi}_{+,j,k} \otimes \phi_{,j,l} \rangle \phi_{-,j,k}(x)\phi_{j,l}(y) \end{Bmatrix} \tag{38}$$

This vector-valued projection is written alternatively as

$$\boldsymbol{Q}_j \boldsymbol{f} \equiv \begin{Bmatrix} Q^{(2)}_j f_1 \\ Q^{(1)}_j f_2 \end{Bmatrix} \tag{39}$$

Up until this point, no effort has been made to characterize the divergence-free functions within $\boldsymbol{V}_j$. Divergence-free subspaces $\boldsymbol{H}$ of $\boldsymbol{V}_j$ can be determined with the introduction of a carefully chosen set of vector-valued basis functions $\boldsymbol{\psi}_{e,i}$. For each of the vertices $e \in E^* = \{(e_1, e_2) : e_i \in \{0, 1\}\} \sim (0, 0)$, and for each integer $i \neq i_e$, we define

$$\boldsymbol{\psi}_{e,i} = \begin{cases} 0, & j \notin \{i, i_e\} \\ \psi^{(\sim i)}_e, & j = i \\ -\frac{1}{4}\frac{\partial}{\partial x_i}\left(\psi^{(\sim i, \sim i_e)}_e\right), & j = i_e \end{cases} \tag{40}$$

In Eq. (40), the symbol $\sim i$ is interpreted as not i, or the complement of i. Note that this notation employs a redundant numbering of the basis for the vector space $\boldsymbol{H}$. That is, there are only particular combinations of (e, i) that are permissible in the preceding definition. In two dimensions, there are precisely three vectors corresponding to the pairs:

$$(e, i) = [(1, 0), 2], [(0, 1), 1], [(1, 1), 2] \tag{41}$$

These three basis vectors are given hereafter for $(e, i) = [(1, 0), 2]$

$$\boldsymbol{\psi}_{(1,0),2} = \begin{Bmatrix} -\frac{1}{4}\psi(x)\phi'(y) \\ \psi_-(x)\phi(y) \end{Bmatrix} = \begin{Bmatrix} -\frac{1}{4}\psi(x)\phi'(y) \\ \frac{1}{4}\psi'(x)\phi(y) \end{Bmatrix} \tag{42}$$

for $(e, i) = [(0, 1), 1]$

$$\boldsymbol{\psi}_{(0,1),1} = \begin{Bmatrix} \phi(x)\psi_-(y) \\ -\frac{1}{4}\phi'(x)\psi(y) \end{Bmatrix} = \begin{Bmatrix} \frac{1}{4}\phi(x)\psi'(y) \\ -\frac{1}{4}\phi'(x)\psi(y) \end{Bmatrix} \tag{43}$$

and for $(e, i) = [(1, 1), 2]$

$$\boldsymbol{\psi}_{(1,1),2} = \begin{Bmatrix} -\frac{1}{4}\psi(x)\psi'(y) \\ \psi_-(x)\psi(y) \end{Bmatrix} = \begin{Bmatrix} -\frac{1}{4}\psi(x)\psi'(y) \\ \frac{1}{4}\psi'(x)\psi(y) \end{Bmatrix} \tag{44}$$

Exactly as in the case of the scalar bases, we define the translates and dilates of the vector bases to be

$$\boldsymbol{\psi}_{e,i,j,K}(x, y) = 2^j \boldsymbol{\psi}_{e,i}\left(2^j x - k_1, 2^j y - k_1\right) \tag{45}$$

where $K = (k_1, k_2)$ is a pair of translation values for the x direction and y direction. The normalization 2^j follows because each vector basis is comprised of a product of scalar basis functions in the x and y. It is clear that each of these vector-valued functions is divergence free,

$$\operatorname{div} \boldsymbol{\psi}_{(1,0),2} = \operatorname{div} \boldsymbol{\psi}_{(0,1),1} = \operatorname{div} \boldsymbol{\psi}_{(1,1),2} = 0 \tag{46}$$

Thus, although the presentation of the framework is somewhat lengthy, we can now present the most essential tool in deriving wavelet-based postprocessing methods. The following theorem due to Lemarie-Rieusset[27–29] shows that these divergence-free vectors generate a basis for the subspace consisting of the divergence-free vectors in $\boldsymbol{V}_j - \boldsymbol{V}_{j-1}$.

Theorem: For each $e \in E^*$, we have that the divergence of the projection is equal to the projection of the divergence:

$$\nabla \cdot (\boldsymbol{Q}_{j,e}\boldsymbol{f}) = \nabla \cdot \begin{Bmatrix} Q^{(2)}_{j,e} f_1 \\ Q^{(1)}_{j,e} f_2 \end{Bmatrix} = Q^{(1,2)}_{j,e}(\nabla \cdot f) \tag{47}$$

In addition, for every $\boldsymbol{f} \in \boldsymbol{H}$, we have a unique expansion:

$$\begin{Bmatrix} Q^{(2)}_{j,e} f_1 \\ Q^{(1)}_{j,e} f_2 \end{Bmatrix} = \sum_{i \neq i_e} \sum_{K=(k_1,k_2)} \langle \boldsymbol{f}, \tilde{\psi}_{e,i,j,K} \boldsymbol{e}_i \rangle \psi_{e,i,j,K} \tag{48}$$

$$\boldsymbol{Q}_j \boldsymbol{f} = \sum_{e \in E^*} \sum_{i \neq i_e} \sum_{K=(k_1,k_2)} \langle \boldsymbol{f}, \tilde{\psi}_{e,i,j,K} \boldsymbol{e}_i \rangle \psi_{e,i,j,K} \tag{49}$$

In these equations, $\boldsymbol{e}_i$ is the canonical basis vector with a 1 in the ith location and zeros elsewhere. Some comments follow:

1) The central task of this paper then, is to derive specific implementations of the rather abstract projection operators in Eqs. (47–49) that are applicable for postprocessing particle image velocimetry data.

2) The choice of filter implementations discussed in the next section is driven by the form of the compatibility conditions in Eqs. (19) and (20). That is, a pragmatic realization of the multilevel projections in Eqs. (19–49) is achieved provided we can find dual multiresolutions whose generators satisfy Eqs. (19) and (20).

3) Interested readers of this paper may define alternative postprocessing methods for PIV based on alternative wavelet systems. The properties desirable of these methods would include a) short support and b) simple boundary conditions.

Filter Implementation

From considerations in the last section, we see that the construction of divergence-free wavelets relies on the selection of the dual pairs ϕ and $\tilde{\phi}$ and ϕ_- and ϕ_+. In this paper, we choose

$$\phi(x) = N_3(x), \qquad \phi_-(x) = N_2(x) \tag{50}$$

where $N_m(x)$ is the mth-order cardinal B spline. It is well known that[32]

$$N'_m(x) = N_{m-1}(x) - N_{m-1}(x-1) \tag{51}$$

for any B spline of order m. Consequently, the critical condition (17) is satisfied.

We must now choose some scaling function $\tilde{\phi}$ that is dual to $N_3(x)$ and a second scaling function ϕ_+ that is dual to ϕ_-, such that the conditions of proposition (18) are satisfied. It is known that there are many generators that define multiresolution analyses that are dual to either $\phi(x) = N_3(x)$ or $\phi_-(x) = N_2(x)$. The Laurent series symbols for $\phi(x) = N_3(x)$ and $\phi_-(x) = N_2(x)$ are given by

$$a(z) = \tfrac{1}{8}(z^{-1} + 3z^0 + 3z + z^2), \qquad a_-(z) = \tfrac{1}{4}(z^{-1} + 2 + z) \tag{52}$$

Potential choices for dual multiresolution analyses are given in Table (6.1) in Ref. 25. Fortunately, we can choose a generator $\tilde{\phi}$ with symbol

$$\tilde{a}(z) = \tfrac{3}{64}z^{-3} - \tfrac{9}{64}z^{-2} - \tfrac{7}{64}z^{-1} + \tfrac{45}{64}z^0 + \tfrac{45}{64}z^1 - \tfrac{7}{64}z^2 - \tfrac{9}{64}z^3 + \tfrac{3}{64}z^4 \tag{53}$$

that is dual to $\phi(x)$ and a generator $\phi_+(x)$ with symbol

$$a_+(z) = \tfrac{3}{128}z^{-4} - \tfrac{3}{64}z^{-3} - \tfrac{1}{8}z^{-2} + \tfrac{19}{64}z^{-1} + \tfrac{45}{64}z^0 + \tfrac{19}{64}z - \tfrac{1}{8}z^2 - \tfrac{3}{64}z^3 + \tfrac{3}{128}z^4 \tag{54}$$

that is dual to $\phi_-(x)$, such that the conditions of proposition (24) hold. For example, we have

$$(1 + z^{-1})\tilde{a}(z) = 2a_+(z) \tag{55}$$

by inspection. Figure 1 shows our choice of B-spline functions that will be used in subsequent experiments. Based on these B-spline functions and the derivation of the divergence-free vector functions in the preceding section, the following divergence-free vector functions are chosen as our basis

$$\begin{aligned}
\phi(x,y) &= \begin{Bmatrix} N_3(x)N'_3(y) \\ -N'_3(x)N_3(y) \end{Bmatrix} \\
\psi_{(0,1),1}(x,y) &= \begin{Bmatrix} \frac{1}{4}N_3(x)\psi'_3(y) \\ -\frac{1}{4}N'_3(x)\psi_3(y) \end{Bmatrix} \\
\psi_{(1,0),2}(x,y) &= \begin{Bmatrix} -\frac{1}{4}\psi_3(x)N'_3(y) \\ \frac{1}{4}\psi'_3(x)N_3(y) \end{Bmatrix} \\
\psi_{(1,1),2}(x,y) &= \begin{Bmatrix} -\frac{1}{4}\psi_3(x)\psi'_3(y) \\ \frac{1}{4}\psi'_3(x)\psi_3(y) \end{Bmatrix}
\end{aligned} \tag{56}$$

In the following, the two-scale equations for the preceding vector functions are derived. Let us assume that we have the following two-scale equations for the B splines just introduced:

$$\begin{aligned}
N_3(x) &= \sum_k a^3_k N_3(2x-k), \qquad \psi_3(x) = \sum_k b^3_k N_3(2x-k) \\
N_2(x) &= \sum_k a^2_k N_2(2x-k), \qquad \psi_2(x) = \sum_k b^2_k N_2(2x-k)
\end{aligned} \tag{57}$$

Then the two-scale equation for the vector-valued scaling functions are derived as

$$\begin{aligned}
\phi(x,y) &= \begin{Bmatrix} N_3(x)N'_3(y) \\ -N'_3(x)N_3(y) \end{Bmatrix} \\
&= \begin{Bmatrix} \left[\sum a^3_k N_3(2x-k)\right]\left[\sum 2a^3_l N'_3(2y-l)\right] \\ -\left[\sum 2a^3_m N'_3(2x-m)\right]\left[\sum a^3_n N_3(2y-n)\right] \end{Bmatrix} \\
&= \sum_{k,l} 2a^3_k a^3_l \phi(2x-k, 2y-l) \equiv \sum_{k,l} A_{k,l}\phi(2x-k, 2y-l)
\end{aligned} \tag{58}$$

In similar manner, the two-scale equation for other functions are obtained as

$$\begin{aligned}
\psi_{(0,1),1}(x,y) &= \sum_{k,l} \frac{1}{2} a^3_k b^3_l \phi(2x-k, 2y-l) \\
&\equiv \sum_{k,l} B^1_{k,l}\phi(2x-k, 2y-l) \\
\psi_{(1,0),2}(x,y) &= \sum_{k,l} \frac{1}{2} b^3_k a^3_l \phi(2x-k, 2y-l) \\
&\equiv \sum_{k,l} B^2_{k,l}\phi(2x-k, 2y-l) \\
\psi_{(1,1),2}(x,y) &= \sum_{k,l} \frac{1}{2} b^3_k b^3_l \phi(2x-k, 2y-l) \\
&\equiv \sum_{k,l} B^3_{k,l}\phi(2x-k, 2y-l)
\end{aligned} \tag{59}$$

Figure 2 presents vector plots for the preceding vector-valued scaling and wavelet functions.

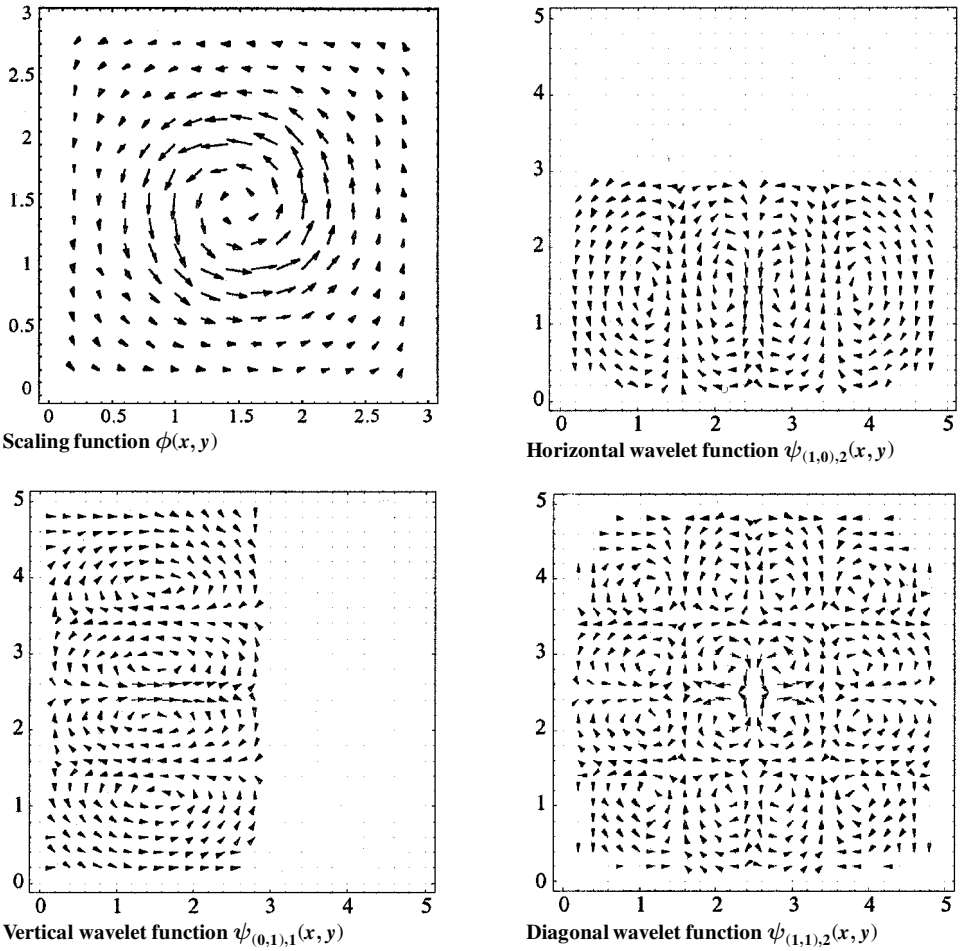

Fig. 2 Vector plots of divergence-free basis functions.

Application to Experimental Flow Diagnostics

Motivation

The use of synthetic or zero mass flux actuators for flow separation control is currently being addressed by many researchers. Current research includes investigation of the performance of this technology for modifying the lift, drag, and flight control characteristics of unconventional airfoils as well as flow separation over bluff bodies.[33,34]

An experimental setup has been developed to study a new type of synthetic jet application to flow control. The idea is to delay the occurrence of flow separation over a curved surface by first removing low-momentum fluid from the boundary layer (suction part of the actuator oscillation period), then reenergizing it and injecting it as high-momentum fluid back into the boundary layer (blowing part of the period), taking advantage of the Coanda effect. The setup incorporating the synthetic jet actuator is schematically shown in Fig. 3. The synthetic jet is housed inside a hollow cylinder and is composed of an almost enclosed cavity, one end of which is covered by an oscillating membrane driven by a dynamic shaker with variable frequency and amplitude of oscillation. The cylinder wall with a slot machined parallel to the cylinder axis covers the other cavity end. Note that the flow does not exit the slot radially. In fact, the actuator is designed in such a way that it takes advantage of the Coanda effect, causing the flow exiting the slot to be almost tangential to the cylinder wall. Besides the momentum addition into the boundary layer, another mechanism that is expected to aid in the separation delay is based on the high receptivity of the shear layer emanating from the point of separation, as demonstrated by previous efforts[35,36] through the use of oscillatory blowing.

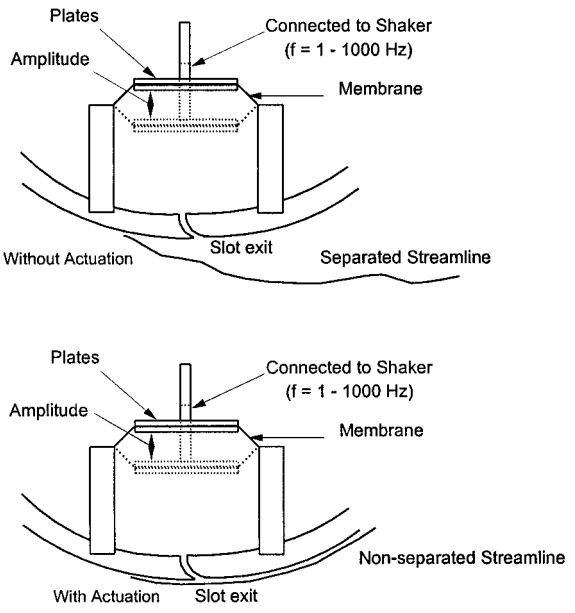

Fig. 3 Schematic of separation control principle via a synthetic jet slot actuator.

Experimental Setup

In the experimental setup, the cylinder was placed between two flat plates, one upstream of the cylinder, the other downstream of it, so that only half of the cylinder was in the flow (Fig. 4). This assembly was then introduced into the test section (cross-sectional dimensions: 150 × 150 mm) of a water tunnel in such a way that the two flat plates and the bottom half of the cylinder formed the top boundary of the measurement domain, whereas the floor of the test section formed the bottom boundary of the domain. The flow entered the domain from the left. The diameter of the cylinder was 102 mm and spanned the entire test section. The water tunnel was set to operate at a freestream velocity of 65 mm/s. The Reynolds number based on the cylinder diameter was 6600.

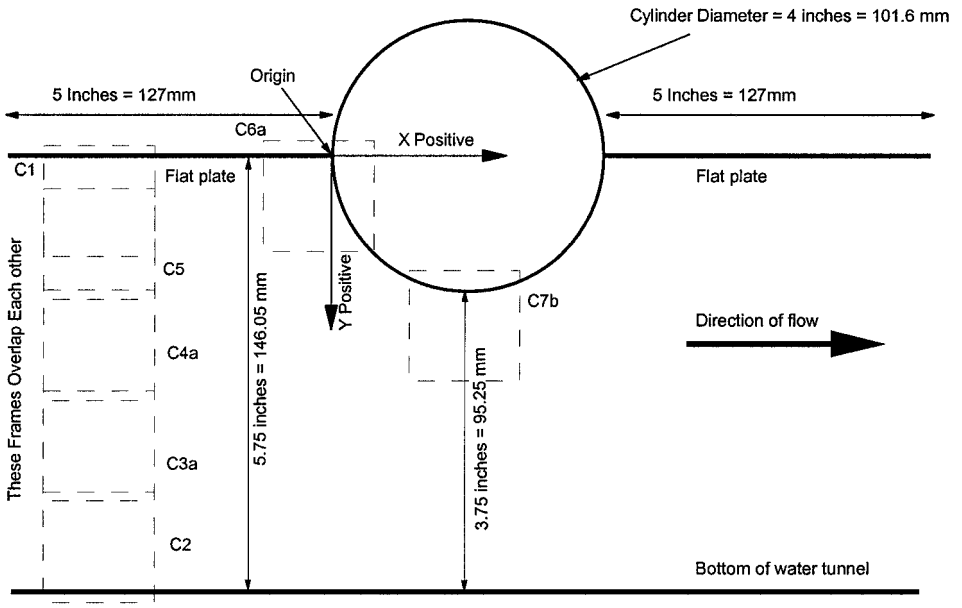

Fig. 4 Schematic of experimental setup.

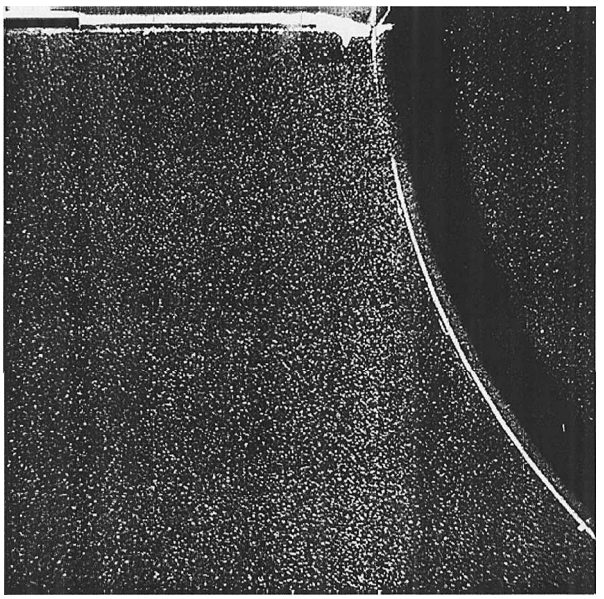

Fig. 5 Typical image used for PIV analysis corresponding to position C6a.

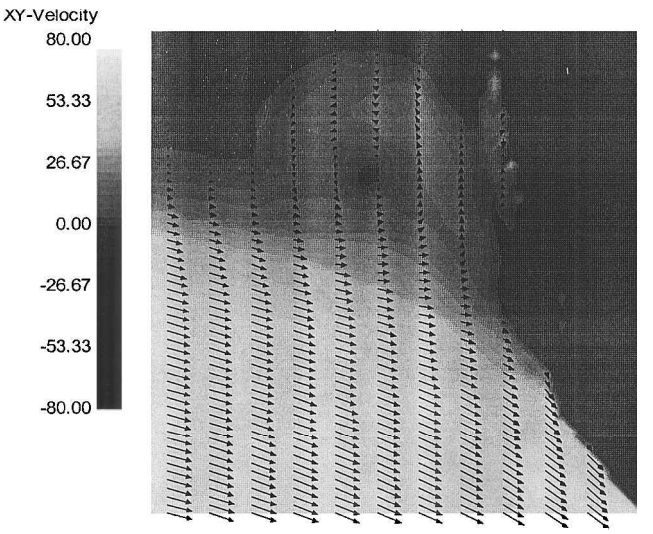

Fig. 6 Velocity field corresponding to position C6a, obtained using cross-correlation algorithms with a 32 × 32 window and an 8 × 8 step; velocity magnitude in millimeters per second.

Figure 4 shows a schematic of the experimental setup that was used during this first phase of the experimental work, which consisted of the initial documentation of the flowfield without the use of any actuators. The flowfield was illuminated using a 25 W continuous wave argon-ion laser. A laser sheet with a thickness of 0.5 mm was produced by means of an array of mirrors and cylindrical lenses. This laser sheet was oriented perpendicular to the tunnel floor to permit documentation of slices of the flowfield parallel to the freestream (two-dimensional flow). The flowfield was seeded with silicon carbide particles (TSI-10081) with a mean diameter of 1.5 μm.

High-frame-rate PIV measurements were performed using a Photec Phantom V3.0 charge-coupled device camera placed normal to the light sheet, operating with a frame rate of 500 fps. The actual image resolution for the digital images recorded at that frame rate was 512 × 512 pixels. The camera was focused onto an area of 40 (horizontal) × 40 mm (vertical), with the position of the image coinciding with the positions shown in Fig. 4. The initial experimental work presented herein includes the documentation of the flowfield near the junction of the cylinder with the flat plate (C6a).

Figure 5 shows a typical particle image acquired at position C6a. Figure 6 shows the flowfield for the same position, which was generated using cross-correlation-based PIV algorithms with an interrogation window size of 32 × 32 and a 8 × 8 step. To facilitate viewing of the vector plot, not all of the velocity vectors are plotted in Fig. 6. Note that the velocity vectors calculated near the solid surfaces of the measurement volume (i.e., near the flat plate or the cylinder surface) tend to be erroneous. This is due to the interrogation window for which the cross correlation was calculated, at that position, containing a section of the cylinder or flat plate surface in it. The glare generated from the laser light reflected on the solid surfaces contributed to the error. Note that for the case of position C6a, the experimental data show the formation of a large recirculation area immediately upstream of the junction point between the flat plate and the cylinder.

Wavelet-Based Compression of Velocity Field

Suppose that we have the following discrete velocity distribution obtained from the PIV experiments:

$$\boldsymbol{u}(x, y) = \sum_{k,l} \begin{Bmatrix} u^x_{k,l} \\ u^y_{k,l} \end{Bmatrix} \tag{60}$$

where $u^x_{k,l}$ and $u^y_{k,l}$ are velocity component at location index (k, l) for the x direction and for the y direction, respectively. Starting from the given discrete velocity data, we first project them onto the subspace of divergence-free scaling functions

$$\boldsymbol{u}_J(x, y) \equiv \sum_{K=(k_1,k_2)} u_{J,K}\phi_{J,K}(x, y) \tag{61}$$

where the superscript J denotes the approximation resolution, or the mesh size 2^{-J}. In the present study, the projection onto the scaling space is realized by using recursive least square algorithm. That is, the coefficients of Eq. (61) are obtained such that the discrete error, $\|\boldsymbol{u}(x, y) - \boldsymbol{u}_J(x, y)\|_{l_2}$, is minimized. Although some sort of interpolation/quadrature method is highly desirable from a practical standpoint, we believe that the derivation of such a practical algorithm will exceed the scope of this paper due to the length limit and should be discussed in detail in another place. In the preceding equations, note that the scalar coefficients $u_{J,K}$ and the dilations and translations of the vector-valued basis functions

$$\phi_{j,K} \equiv 2^j\phi\left(2^j x - k_1, 2^j y - k_2\right), \qquad K = (k_1, k_2) \tag{62}$$

are used in linear combination to represent the vector field. Once we obtain the finest level of projection onto the scaling subspace, the projected flowfield is decomposed into larger-scale (coarse-grid) scaling subspaces and wavelet subspaces such as

$$\begin{aligned}\boldsymbol{u}_J(x, y) &= \boldsymbol{u}_{J-1}(x, y) + \boldsymbol{w}_{1,J-1}(x, y) + \boldsymbol{w}_{2,J-1}(x, y)\\ &\quad + \boldsymbol{w}_{3,J-1}(x, y) = \sum_{K=(k_1,k_2)} u_{J-1,K}\phi_{J-1,K}(x, y)\\ &\quad + \sum_{K=(k_1,k_2)} w_{1,J-1,K}\psi_{(0,1),1,J-1,K}(x, y)\\ &\quad + \sum_{K=(k_1,k_2)} w_{2,J-1,K}\psi_{(1,0),2,J-1,K}(x, y)\\ &\quad + \sum_{K=(k_1,k_2)} w_{3,J-1,K}\psi_{(1,1),2,J-1,K}(x, y)\end{aligned} \tag{63}$$

where wavelet coefficients $\{w_{r,J-1,K},\ r = 1, 2, 3\}$ represent detail information of the original distribution and the scaling coefficients $u_{J-1,K}$ contain coarse-grid information. Continuing the preceding wavelet decomposition, we subsequently obtain

$$\begin{aligned}\boldsymbol{u}_J(x, y) &= \sum_{K=(k_1,k_2)} u_{J_0,K}\phi_{J_0,K}(x, y)\\ &\quad + \sum_{j=J_0}^{J-1}\sum_{K=(k_1,k_2)} \{w_{1,j,K}\psi_{(0,1),1,j,K}(x, y)\\ &\quad + w_{2,j,K}\psi_{(1,0),2,j,K}(x, y) + w_{3,j,K}\psi_{(1,1),2,j,K}(x, y)\}\end{aligned} \tag{64}$$

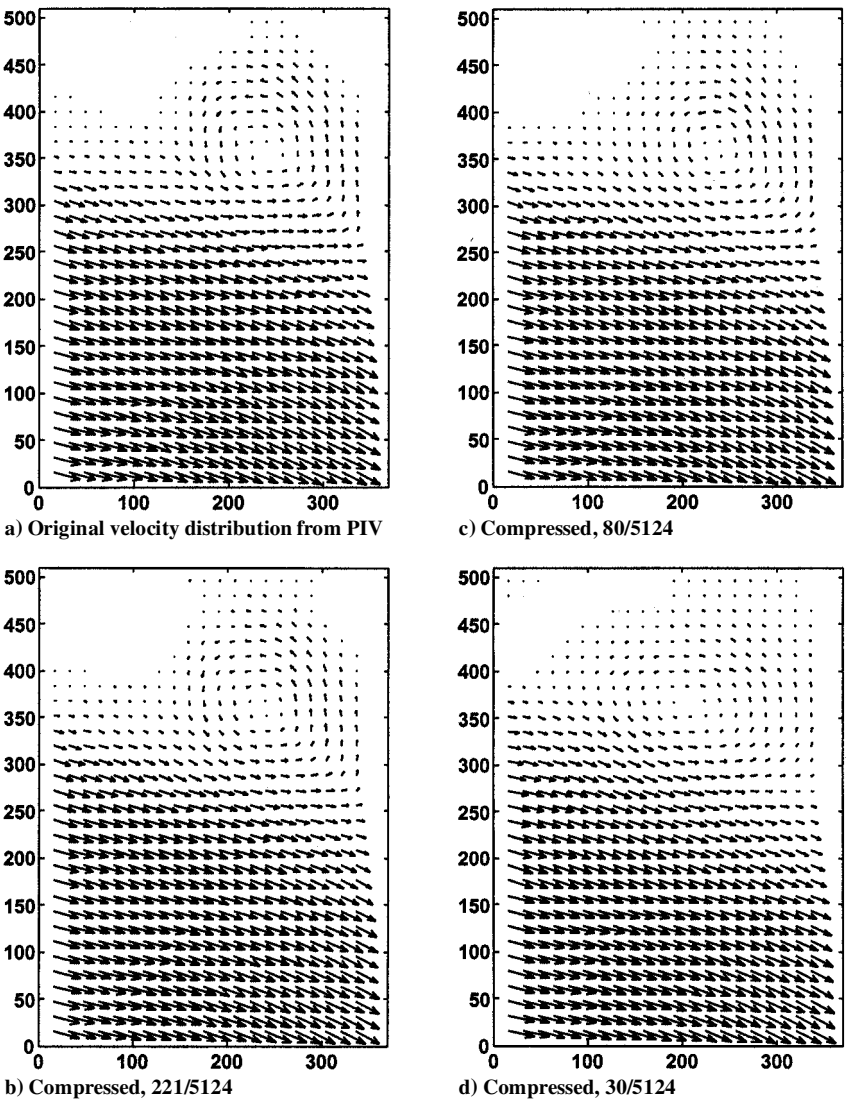

Fig. 7 Compressed velocity fields at various compression ratios.

As mentioned earlier, the coarsest-level scaling coefficients $u_{J_0,K}$ contain larger-scale information of the velocity fields, and the wavelet components $\{w_{r,j,K},\ r = 1, 2, 3\}$ represent detail information at different scales j. After achieving this multilevel decomposition of the original velocity field, the compression is performed by thresholding some or all of the wavelet/scaling coefficients. The thresholding values need to be selected judiciously so that the resulting compressed velocity field retains required/necessary characteristics of the original flowfield, such as location, movement, and strength of vortices, shear layer strength and behavior, etc. For the case of image compression, a rigorous development of the relation between compression error and ratio is presented in Ref. 4. In our present study, we employ a rather trivial and simple thresholding as our initial compression strategy. As shown in the following section, in our first step, we throw away all of the wavelet coefficients, that is, $w_{r,j,K}$ in Eq. (64) thus achieving maximal compression ratio. By doing so, however, we lose a great deal of information because the wavelet coefficients usually carry detail information. Thus, in our next step, we will show that by retaining only those wavelet coefficients at the coarsest level, which are larger than a predetermined value, we are able to reduce the compression error significantly. Certainly, a thorough investigation of thresholding strategy relevant to a reduced-order flow model is necessary and should follow the current study.

Results and Discussion

As an application of the techniques developed herein, a compression of velocity fields obtained from PIV experiments is presented in this section. The velocity field presented in Fig. 6 was first cropped for two reasons: 1) to eliminate erroneous vectors close to the solid surfaces and 2) to achieve a rectangular velocity domain (no curved boundaries, such as the cylinder surface), which is necessary for the application of the present wavelet procedures (this can be avoided by employing different families of wavelets such as those derived in Ref. 37, which has short support and, thus, can accommodate curved boundaries). The resulting velocity field is shown in Fig. 7a. In Fig. 7 and subsequent velocity vector plots, note that only a quarter of the original velocity vectors are plotted for clarity. We utilize the divergence-free wavelet/scaling functions derived earlier.

The original flowfield (Fig. 7a) has 42×61 grid points; thus, we have $2 \times 42 \times 61 = 5124$ velocity data (x and y velocity components at each grid point). Figures 7b–7d present results of wavelet-based compression of the original flowfield at different compression ratios. These compressions are achieved by keeping only scaling function coefficients at each decomposition. That is, the original velocity field $\boldsymbol{u}(x, y) \approx \boldsymbol{u}_J(x, y)$ is approximated by $\boldsymbol{u}_{J-1}(x, y)$, $\boldsymbol{u}_{J-2}(x, y)$, $\boldsymbol{u}_{J-3}(x, y)$, and $\mathbf{u}_{J-4}(x, y)$. As shown in Fig. 7, numbers of coefficients retained are 736, 221, 80, and 30, respectively. That is, only 30 vector functions are used to represent the vector field in Fig. 7d, for example (a compression ratio of $5124/30 = 170.8$). Figures 8–11 show the relative differences between the projected velocity fields and the compressed velocity fields for each of the velocity components

$$\frac{\left|u^x_{\text{compressed},k,l} - u^x_{\text{projected},k,l}\right|}{\max\left|\boldsymbol{u}_{\text{projected},k,l}\right|} \times 100$$

$$\frac{\left|u^y_{\text{compressed},k,l} - u^y_{\text{projected},k,l}\right|}{\max\left|\boldsymbol{u}_{\text{projected},k,l}\right|} \times 100 \tag{65}$$

at various compression ratios. Here, by projected we indicate the flowfield that results from the projection of the original data onto the wavelet space, before any thresholding occurs. Small differences exist between the original and projected flowfields. These differences are attributed mostly to the projected flowfield being automatically divergence-free because it is projected on a divergence-free basis, whereas the original flowfield is not identically divergence-free (although it should be) due to experimental errors. Therefore, the projected flowfield is, in a sense, a more physically correct representation. Note, especially in Figs. 11b and 11d, that the error levels are high along the shear layer (the boundary between the vortex in the upper section and the potential flow below it). Keeping in mind that the wavelets are the functions that capture

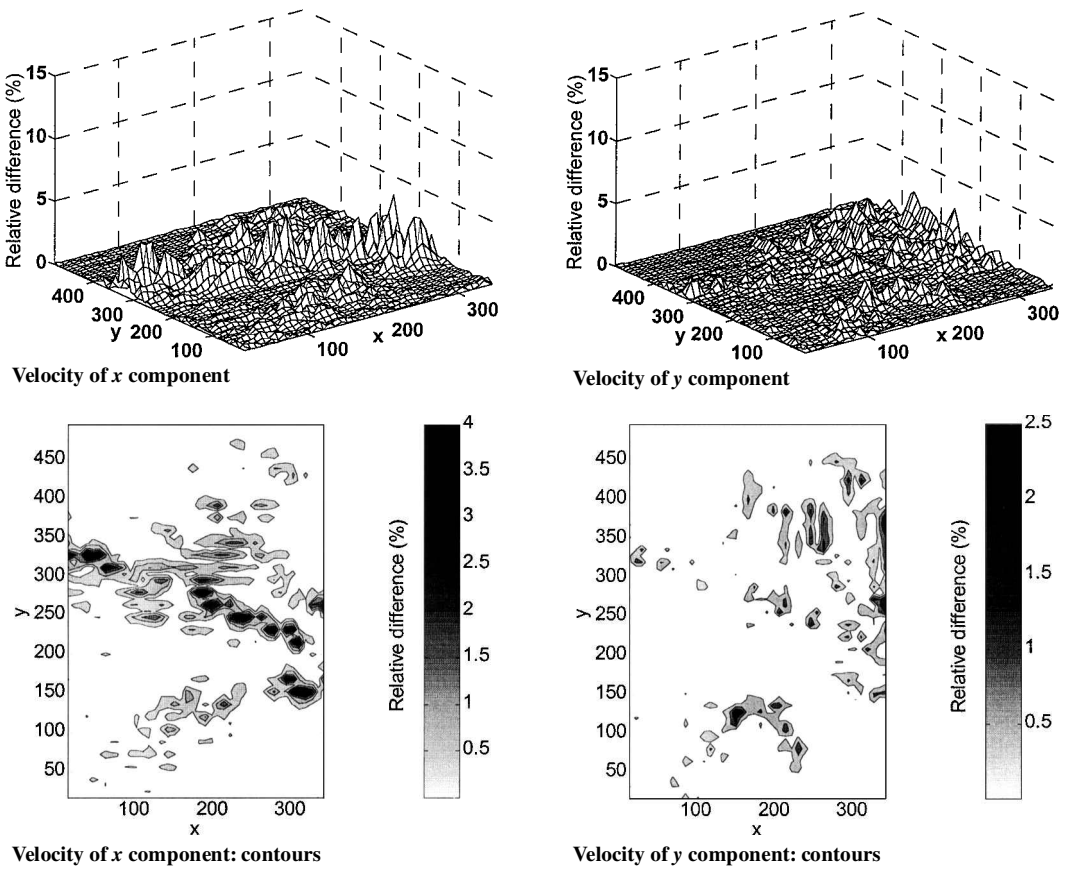

Fig. 8 Relative difference from projected velocity in percentage (compressed, 736/5124).

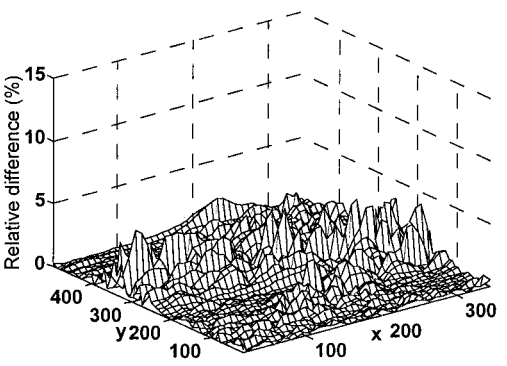

Velocity of *x* component

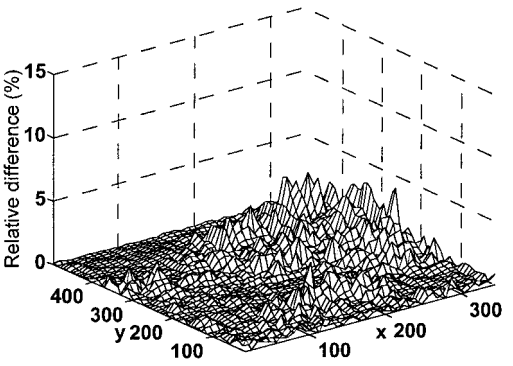

Velocity of *y* component

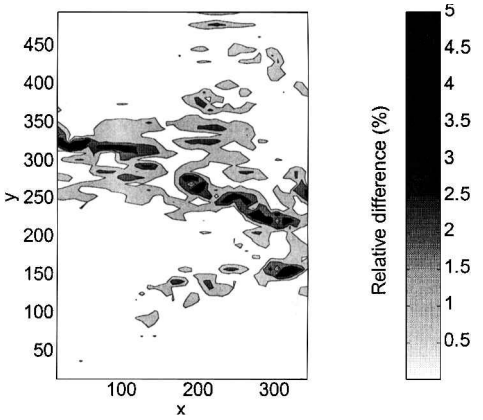

Velocity of *x* component: contours

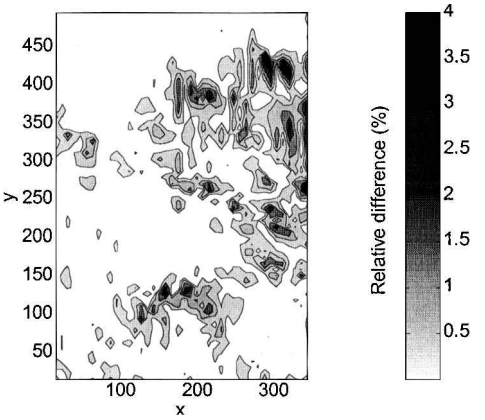

Velocity of *y* component: contours

Fig. 9 Relative difference from projected velocity in percentage (compressed, 221/5124).

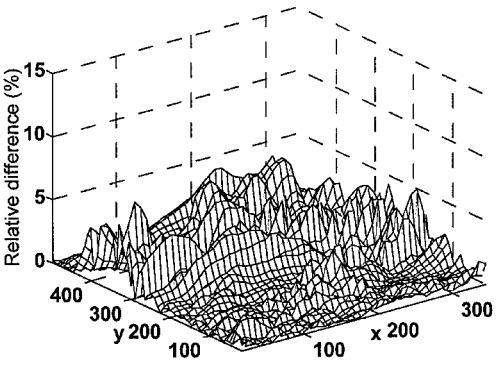

Velocity of *x* component

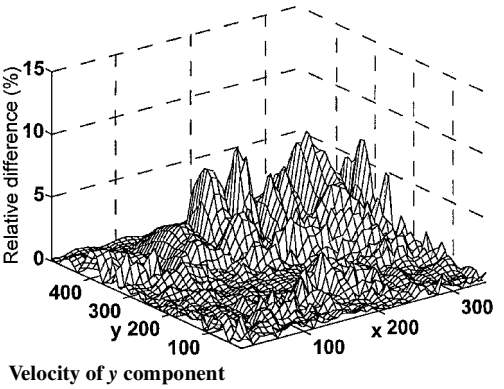

Velocity of *y* component

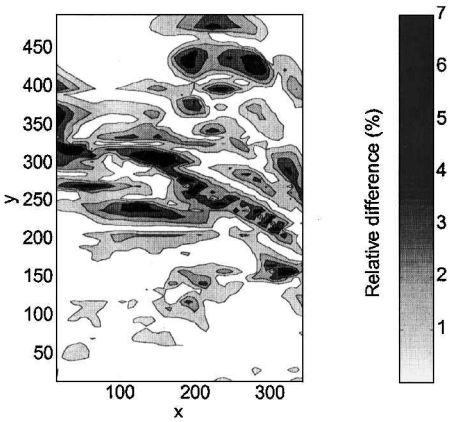

Velocity of *x* component: contours

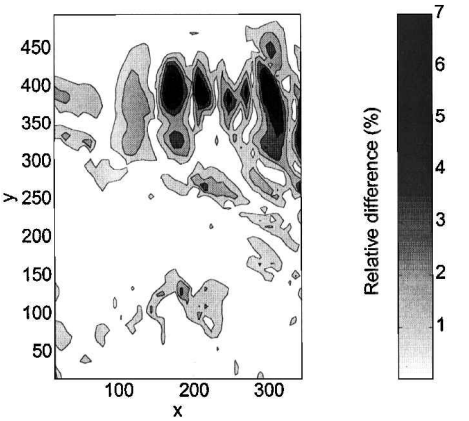

Velocity of *y* component: contours

Fig. 10 Relative difference from projected velocity in percentage (compressed, 80/5124).

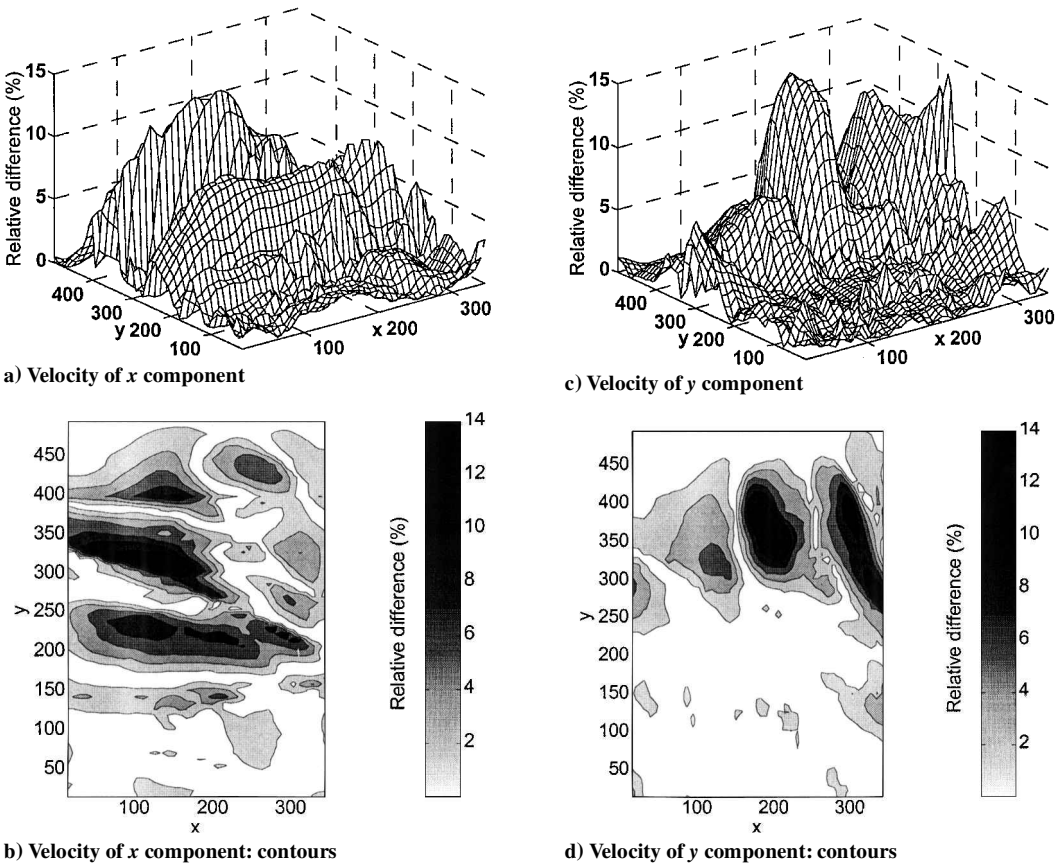

Fig. 11 Relative difference from projected velocity in percentage (compressed, 30/5124).

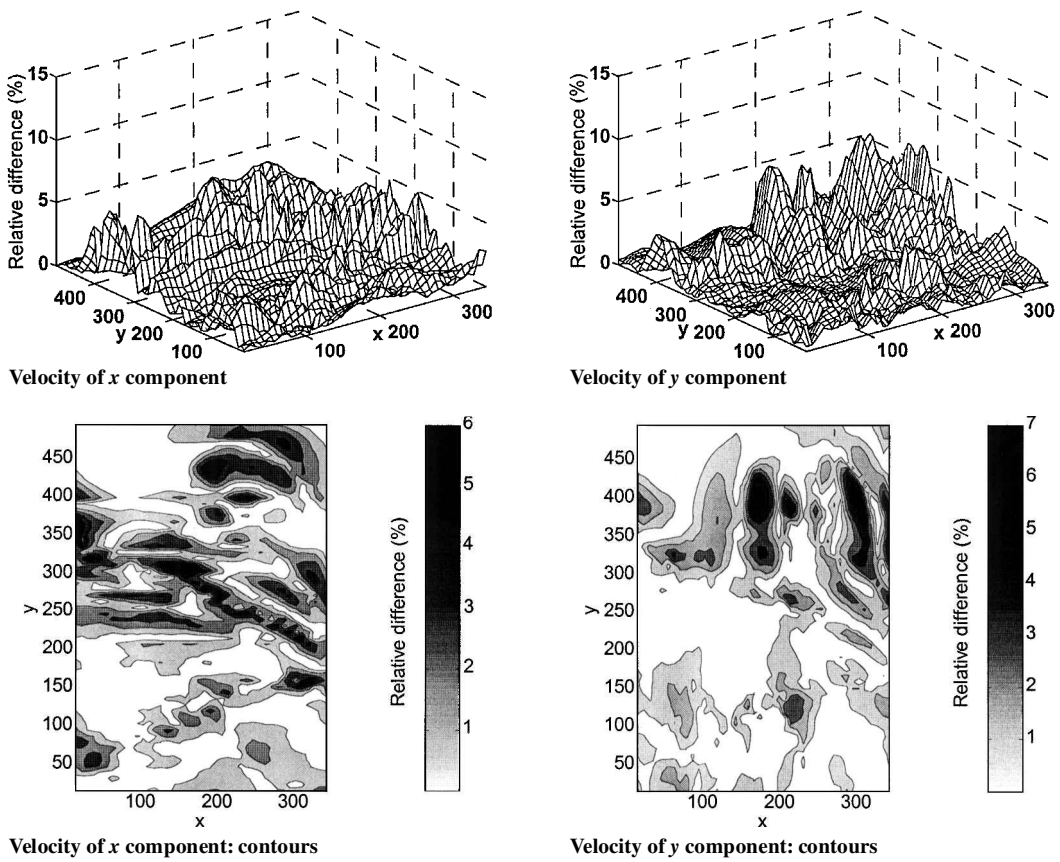

Fig. 12 Relative difference from projected velocity in percentage after adding wavelet components to Fig. 12 (compression ratio = 5124/58, relative l_2 error = 3.9908%).

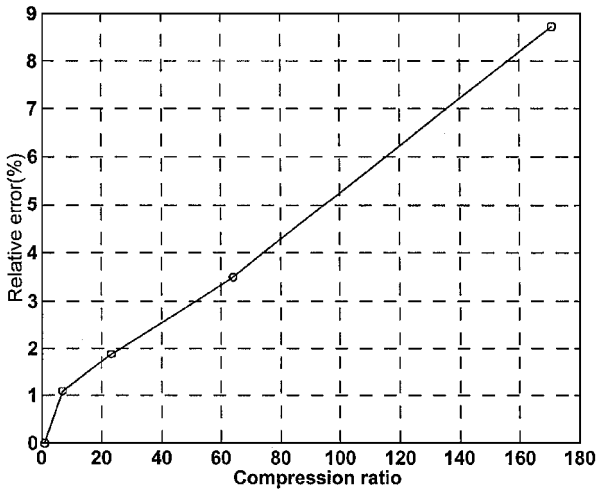

Fig. 13 Relative l_2 difference from projected velocity for different compression ratios.

the flow details, that is, the fine-scale flow features, this is consistent with our throwing away all of the wavelet coefficients. When we include some of the wavelet coefficients through thresholding, the resulting error can be significantly reduced. Figure 12 shows an example of such cases. Some (not all) of the wavelet coefficients at level $J-4$, $\{w_{r,J-4,K},\ r=1, 2, 3\}$, are added to $\boldsymbol{u}_{J-4}(x, y)$, and the resulting error distribution is shown in Fig. 12. Specifically, 28 wavelet coefficients are added to 30 scaling coefficients, resulting in a compression ratio of $5124/58 = 88.34$. Comparing Fig. 12 to Fig. 11, we observe that the errors are reduced significantly. In this example, we have included wavelet coefficients only at the coarsest level, but this can be done at each decomposition level for achieving compression with reduced error distribution. For comparison, relative l_2 differences

$$\frac{|\boldsymbol{u}_{\text{compressed}} - \boldsymbol{u}_{\text{projected}}|_{l_2}}{|\boldsymbol{u}_{\text{projected}}|_{l_2}} \times 100 \tag{66}$$

at different compression ratios are shown in Fig. 13.

While the preceding results for a selected flowfield are convincing, the readers may argue the limited nature of the examples provided in this paper. The authors would like to mention that exactly the same methodology has been applied to more complicated synthetic jet flowfields, and that similar results were obtained. We regret, however, that due to the length limit of the paper, the results are published elsewhere. Interested readers are referred to Rediniotis et al.[38]

Conclusions

This paper has presented a methodology by which reduced-order, divergence-free representations of flowfields can be obtained. The results, though preliminary, are promising; compression ratios of two orders of magnitude are obtainable depending on the flow under consideration. Still, there are several open issues that must be resolved in the current technique, and these merit further study. Because of the large supports of these functions, we have to keep additional functions in the vicinity of the boundaries, and, thus, we suffer a deterioration in compression ratios. However, we still obtain a superior compression ratio as observed in our results. The method is semi-automated and achieved via fast-filtering implementation of divergence-free wavelets. The full automation of this algorithm requires systematic methods for the determination of thresholding techniques based on the physics of the flow. Moreover, it is imperative that the relative merits of the method be gauged in comparison to other techniques, including proper orthogonal decomposition methods.

Acknowledgments

This work was supported by the Office of Naval Research under Contract N000014-97-1-0943. Special thanks go to Allen Moshfegh, the Technical Monitor of the program, for his support. The authors would also like to thank Jose Gilarranz and Brian Moeller for their help with the experiments.

References

[1]Daubechies, I., "Orthonormal Bases of Compactly Supported Wavelets," *Communications on Pure and Applied Mathematics*, Vol. 41, No. 7, 1988, pp. 909–996.

[2]Chui, C. K. (ed.), *Wavelets: A Tutorial in Theory and Applications*, Academic, San Diego, CA, 1992, pp. 541–700.

[3]Mallat, S., "A Theory for Multiresolution Signal Decomposition: The Wavelet Representation," *IEEE Transactions on Pattern Analysis and Machine Intelligence*, Vol. 11, No. 7, 1989, pp. 674–693.

[4]DeVore, R. A., Jawerth, B., and Lucier, B. J., "Image Compression Through Wavelet Transform Coding," *IEEE Transactions on Information Theory, Special Issue on Wavelet Transforms and Multiresolution Signal Analysis*, Vol. 38, No. 2, 1992, pp. 719–746.

[5]Jaffard, S., and Laurencot, P., "Orthonormal Wavelets, Analysis of Operators, and Applications to Numerical Analysis," *Wavelets: A Tutorial in Theory and Applications*, edited by C. Chui, Academic, San Diego, CA, 1992, pp. 543–601.

[6]Ko, J., Kurdila, A. J., Gilarranz, J. L., and Rediniotis, O. K., "Particle Image Velocimetry via Wavelet Analysis," *AIAA Journal*, Vol. 36, No. 8, 1998, pp. 1451–1459.

[7]Farge, M., Schneider, K., and Kevlahan, N., "Non-Gaussianity and Coherent Vortex Simulation for Two-Dimensional Turbulence Using an Adaptive Orthogonal Wavelet Basis," *Physics of Fluids*, Vol. 11, No. 8, 1999, pp. 2187–2201.

[8]Sritharan, S. S. (ed.), *Optimal Control of Viscous Flows*, Society for Industrial and Applied Mathematics, Philadelphia, 1998, pp. 1–198.

[9]Joshi, S. S., Speyer, J. L., and Kim, J., "A Systems Theory Approach to the Feedback Stabilization of Infinitesimal and Finite-Amplitude Disturbances in Plane Poiseuille Flow," *Journal of Fluid Mechanics*, Vol. 332, Feb. 1997, pp. 157–184.

[10]Cortellezi, L., and Speyer, J., "Advance in Boundary Layer Control: Robust Reduced-Order Transition Controller," Computational and Applied Mathematics Rept. 97-57, University of California, Los Angeles, 1997.

[11]Breuer, K. S., Amonlirdviman, K., and Rathnasingham, "Adaptive Feed-Forward Control of Turbulent Boundary Layers," AIAA Paper 98-1025, Jan. 1998.

[12]Loeve, M., "Functions Aleatoire de Second Ordre," *Compte Rendus Acad. Sci. Paris*, Vol. 220, 1945.

[13]Karhunen, K., "Zur Spektral Theorie Stochasticher Prozesse," *Ann. Acad. Sci. Fennicae, Ser. A1*, Vol. 34, 1946.

[14]Lumley, J. L., "The Structure of Inhomogeneous Turbulent Flows," *Atmospheric Turbulence and Radio Wave Propagation*, edited by A. M. Yaglom and V. I. Tatarsky, Nauka, Moscow, 1967, pp. 166–178.

[15]Reichert, R. S., Hatay, F. F., Biringen, S., and Huser, A., "Proper Orthogonal Decomposition Applied to Turbulent Flow in a Square Duct," *Physics of Fluids*, Vol. 6, No. 9, 1994, pp. 3086–3092.

[16]Ly, H. V., and Tran, H. T., "Proper Orthogonal Decomposition for Flow Calculations and Optimal Control in a Horizontal CVD Reactor," Center for Research in Scientific Computation, TR CRSC-TR-98-13, North Carolina State Univ., Raleigh, NC, March 1998.

[17]Tang, K. Y., Graham, W. R., and Peraire, J., "Active Flow Control Using a Reduced Order Model and Optimum Control," *Proceedings of the 27th AIAA Fluid Dynamics Conference*, AIAA, Reston, VA, 1996.

[18]Aubry, N., Holmes, P., Lumley, J. L., and Stone, E., "The Dynamics of Coherent Structures in the Wall Region of a Turbulent Boundary Layer," *Journal of Fluid Mechanics*, Vol. 192, 1988, pp. 115–173.

[19]Ball, K. S., Sirovich, L., and Keefe, L. R., "Dynamical Eigenfunction Decomposition of Turbulent Channel Flow," *International Journal for Numerical Methods in Fluids*, Vol. 12, No. 6, 1991, pp. 585–604.

[20]Berkooz, G., Holmes, P., and Lumley, J. L., "The Proper Orthogonal Decomposition in the Analysis of Turbulent Flows," *Annual Review of Fluid Mechanics*, Vol. 25, 1993, pp. 539–575.

[21]Gunzburger, M. D., *Finite Element Methods for Viscous Incompressible Flows: A Guide to Theory, Practice, and Algorithms*, Academic, Boston, 1989, pp. 108–114.

[22]Ito, K., and Ravindran, S. S., "Reduced Basis Method for Flow Control," Center for Research in Scientific Computation, TR CRSC-TR96-25, North Carolina State Univ., Raleigh, NC, Aug. 1996.

[23]Ito, K., and Ravindran, S. S., "A Reduced Basis Method for Control Problems Governed by PDEs," Center for Research in Scientific Computation, TR CRSC-TR97-1, North Carolina State Univ., Raleigh, NC, Jan. 1997.

[24]Ito, K., and Ravindran, S. S., "A Reduced-Order Method for Simulation and Control of Fluid Flow," *Journal of Computational Physics*, Vol. 143, No. 5, 1998, pp. 403–425.

[25]Cohen, A., Daubechies, I., and Feauveau, J.-C., "Biorthogonal Bases of Compactly Supported Wavelets," *Communications on Pure and Applied Mathematics*, Vol. 45, No. 5, 1992, pp. 485–560.

[26]Daubechies, I., *Ten Lectures on Wavelets*, Society of Industrial and Applied Mathematics, Philadelphia, 1992, pp. 156–166.

[27]Lemarie-Rieusset, P., "Ondelettes Vecteurs a Divergence Nulle," *Comptes Rendus de l'Academie des Sciences Serie I. Mathematique*, Vol. 313, No. 5, 1991, pp. 213–216.

[28]Lemarie-Rieusset, P., "Wavelets, Splines and Divergence-Free Vector Functions," *Approximation Theory, Spline Functions and Applications*, edited by S. P. Singh, Kluwer Academic, Norwell, MA, 1992, pp. 381–390.

[29]Lemarie-Rieusset, P., "Un Theoreme d'Inexistence Pour les Ondelettes Vecteurs a Divergence Nulle," *Comptes Rendus de l'Academie des Sciences Serie I. Mathematique*, Vol. 319, No. 8, 1994, pp. 811–813.

[30]Urban, K., "On Divergence-Free Wavelets," *Advances in Computational Mathematics*, Vol. 4, No. 1, 1995, pp. 51–82.

[31]Urban, K., "Using Divergence Free Wavelets for the Numerical Solution of the Stokes Problem," *Algebraic Multilevel Iterations*, edited by O. Axelsson and B. Polman, Nijmegen Univ., Nijmegen, The Netherlands, 1996, pp. 259–278.

[32]Chui, C. K., *An Introduction to Wavelets*, Academic Press, San Diego, CA, 1992, pp. 81–117.

[33]Amitay, M., Smith B. L., and Glezer, A., "Aerodynamic Flow Control Using Synthetic Jet Technology," AIAA Paper 98-0208, Jan. 1998.

[34]Smith D., Amitay, M., Kibens, V., Parekh, D., and Glezer, A., "Modifications of Lifting Body Aerodynamics Using Synthetic Jet Actuators," AIAA Paper 98-0209, Jan. 1998.

[35]Seifert, A., Bachat, T., Koss, D., Shepshelovich, M., and Wygnanski, I., "Oscillatory Blowing: A Tool to Delay Boundary-Layer Separation," *AIAA Journal*, Vol. 31, No. 11, 1993, pp. 2052–2060.

[36]Seifert, A., and Pack, L. G., "Oscillatory Control of Separation at High Reynolds Numbers," AIAA Paper 98-0214, Jan. 1998.

[37]Donovan, G. C., Geronimo, J. S., and Hardin, D. P., "Intertwining Multiresolution Analyses and the Construction of Piecewise-Polynomial Wavelets," *SIAM Journal of Mathematical Analysis*, Vol. 27, No. 6, 1996, pp. 1791–1815.

[38]Rediniotis, O. K., Ko, J., Yue, X., and Kurdila, A. J., "Synthetic Jets, Their Reduced-Order Modeling, and Applications to Flow Control," AIAA Paper 99-1000, Jan. 1999.

P. Givi
Associate Editor